RSC Advances

PAPER

View Article Online
View Journal | View Issue

Cite this: *RSC Adv.*, 2017, **7**, 5989

Construction of hybrid multi-shell hollow structured CeO_2–MnO_x materials for selective catalytic reduction of NO with NH_3†

Kaili Ma,[ab] Weixin Zou,[ab] Lei Zhang,[c] Lulu Li,[ab] Shuohan Yu,[ab] Changjin Tang,*[ab] Fei Gao[b] and Lin Dong*[ab]

Received 26th October 2016
Accepted 20th December 2016

DOI: 10.1039/c6ra25863h

www.rsc.org/advances

Hollow structured CeO_2–MnO_x hybrid materials with up to three shells were prepared successfully by using carbon spheres as the hard template. It was found that the shells could be well controlled by simply adjusting the calcination rate. Elemental mapping results showed Mn and Ce species exhibited a homogeneous spatial distribution and the existence of Mn could improve the diffusion of CeO_2 into the carbon spheres during the construction of the multi-shell structure, suggesting the intensive cooperative interaction between Mn and Ce. When triple-shell CeO_2–MnO_x hollow spheres were used as a catalyst for selective catalytic reduction of NO with NH_3, superior low-temperature catalytic performance was exhibited, compared with traditional CeO_2–MnO_x nanoparticles, single-shell and double-shell hollow spheres. Combined with XRD, H_2-TPR and XPS characterization, it was indicated that the synergistic effects and surface active species enhanced by the special multi-shell CeO_2–MnO_x hollow structures could account for the excellent performances. The results of the present study shed light on the creation of complex and hybrid hollow structured materials for superior performance in catalysis fields, like NO reduction for environmental protection.

1 Introduction

Ceria, as a typical rare earth oxide, owns considerable intrinsic properties such as abundant oxygen vacancy defects, high oxygen storage capacity and alterable valence states,[1] which result in its extensive applications in the field of diesel soot oxidation,[2] CO oxidation,[3] photocatalysis,[4,5] NO reduction,[6,7] and so on. Nevertheless, pure ceria is rarely used in catalysis due to its inherent poor activity. It is recognized that the combination of CeO_2 and transition as well as noble metals, for instance, Cu,[8] Mn,[6] Nb,[9] Pt[10] and Au,[11] is beneficial to its properties. Besides, manganese hybrid oxides, with variable valences and resulting intrinsic environmentally benign features as well as excellent catalytic activity, have been considered as promising catalysts for redox reactions.[12–14] Thus, much attention has been paid to CeO_2–MnO_x composites due to their admirable performance in catalysis, for example, the low-temperature deNO_x reaction.[6,15,16] The advantageous interactions between Ce and Mn species bring about the excellent redox ability, amphoteric property and thermal stability, which are helpful for the catalytic application of CeO_2–MnO_x composites.[17]

Generally, compared with the irregular particles, catalysts with well-designed structure are supposed to exhibit amazing functions on account of the size, shape, interface effects, *etc.*[18] Thus, considerable researches have been focused on preparing CeO_2–MnO_x composites with specific structures. Chen *et al.* prepared the Ce–Mn binary oxide hollow cubes by a novel method, which obtained excellent CO oxidation activity and remarkable adsorption capacity of Congo red.[19] Putla and the co-workers designed a heteronanostructure of CeO_2 nanocubes (100) with dispersed MnO_x nanoparticles for diesel soot oxidation and continuous-flow benzylamine oxidation.[2] Besides, Wei *et al.* reported a kind of MnO_2 doped CeO_2 catalyst with tailored 3-D channels, which possessed large surface area for chemical absorption, as well as proper channels for diffusion.[20] Hence, the controlled fabrication of well-structured CeO_2–MnO_x composites is of great significance to catalysis field.

Recently, hollow structured materials with features of low density, high permeability and confined inner cavity have captured tremendous attention.[5,21–24] Especially, the fabrication of multi-shell hollow spheres with special isolated chambers and controllable shell structures attracted considerable attention.[25,26] According to the literatures, multi-shell CeO_2 hollow spheres have been successfully synthesized.[4,11,27] Nevertheless, to the best of our knowledge, hybrid multi-shell ceria-based

[a]*Key Laboratory of Mesoscopic Chemistry of MOE, School of Chemistry and Chemical Engineering, Nanjing University, Nanjing 210023, P. R. China. E-mail: tangcj@nju.edu.cn*

[b]*Jiangsu Key Laboratory of Vehicle Emissions Control, Center of Modern Analysis, Nanjing University, Nanjing 210093, P. R. China. E-mail: donglin@nju.edu.cn*

[c]*School of Environmental and Chemical Engineering, Chongqing Three Gorges University, Wanzhou 404000, P. R. China*

† Electronic supplementary information (ESI) available. See DOI: 10.1039/c6ra25863h

hollow spheres with diverse compositions have rarely been prepared, and the relationship of their structure and catalytic performance is not reported yet.

Therefore, in this study, by using carbon spheres as a hard template, we reported for the first time the fabrication of CeO_2–MnO_x hollow spheres with adjustable shells *via* simple modification of calcination rate for the first time. The obtained samples were characterized by scanning electron microscopy (SEM), transmission electron microscopy (TEM), X-ray diffraction (XRD), Brunauer–Emmett–Teller (BET), X-ray photoelectron spectroscopy (XPS), X-ray fluorescence analysis (XRF), H_2-temperature programmed reduction (H_2-TPR) and tested in the reaction of NO reduction by NH_3 (NH_3-SCR). Results showed that Mn and Ce were well distributed on the hybrid hollow spheres, and there existed strong cooperative interaction between Mn and Ce in formation of the multi-shells. In comparison with traditional CeO_2–MnO_x nanoparticles, the multi-shell hollow sphere catalysts exhibited superior low-temperature performance in NH_3-SCR, particularly for the triple-shell sample.

2 Experimental section

2.1 Sample preparation

2.1.1 Materials. All chemicals were of analytical grade (AR), purchased from Sinopharm Chemical Reagent Co., Ltd. (China) and used without further purification.

2.1.2 Synthesis of carbon spheres template. Carbon spheres with the average diameter of about 600 nm were synthesized by our previous report.[28] With 0.2 g CTAB as the surfactant, 2.87 g glucose was dissolved in 30 mL distilled water. Then, a hydrothermal treatment of the above mixed solution at 180 °C for 9 h was taken. After being centrifuged and stepwise washed with distilled water and absolute ethanol, the dark brown precipitate was dried at 60 °C for 6 h in air, and then the carbon spheres were obtained.

2.1.3 Synthesis of multi-shell CeO_2–MnO_x hollow spheres (MSCMHSs). The MSCMHSs were synthesized with the following procedure. Appropriate amounts of $Ce(NO_3)_3 \cdot 6H_2O$, $Mn(NO_3)_2$ aqueous solution (50 wt%) and $NH_4Ac \cdot 2H_2O$ (n_{Ce} : n_{Mn} : $n_{NH_4Ac} = 0.371 : 0.629 : 11.86$) were dissolved together in 20 mL absolute ethanol to form a clear solution, into which 0.2 g carbon spheres were ultrasonically dispersed. Then the dark brown suspension was transferred into a 50 mL Teflon-lined stainless steel autoclave and maintained at 180 °C for 4 h in oven. After it was cooled down, the brown solid product could be collected *via* centrifugation at 10 000 rpm for 5 min, followed by being washed with distilled water and absolute ethanol several times, respectively. The precursor was dried at 80 °C and then calcined in air at 600 °C for 3 h with different defined heating rates (2 °C min^{-1}, 5 °C min^{-1} and 10 °C min^{-1}) to get the anticipated MSCMHSs. Individual cerium and manganese hollow spheres could be synthesized without another raw material. Additionally, traditional CeO_2–MnO_x nanoparticles (NP) with identical molar ratio were also prepared through the same method without carbon spheres (heating rate being of 10 °C min^{-1}) for comparison purposes.

2.2 Characterizations

Scanning electron microscopy (SEM) images were captured on Philips XL30 electron microscope operated at beam energy of 10.0 kV.

Transmission electron microscopy (TEM) images were taken on a JEM-2100 instrument with an acceleration voltage of 200 kV. High-resolution transmission electron microscopy (HRTEM) and selected area electron diffraction (SAED) were determined on a JEM-2100F transmission electron microscope with an accelerating voltage of 200 kV. High-angle annular dark field (HAADF)-STEM characterizations were carried out using a JEOL 2100F microscope equipped with an Oxford energy dispersive X-ray (EDX) analysis system with an acceleration voltage of 200 kV.

Fourier translation infrared spectrum (FT-IR) was collected on a NICOLET iS10 FT-IR spectrometer (Thermo Electron Corporation, USA) from 600 to 4000 cm^{-1}. The number of scans was 32 at a resolution of 4 cm^{-1}.

Powder X-ray diffraction (XRD) patterns were recorded on a Shimadzu XRD-6000 power X-ray diffractometer with Cu Kα radiation ($\lambda = 1.5418$ Å). The intensity data were collected over a 2θ range of 10–80° with a 0.05° step size.

Textural characteristics of the samples were determined by a nitrogen adsorption operation at −196.15 °C on a Micrometrics ASAP-2020 adsorption analyzer by the Brunauer–Emmett–Teller (BET) method. Ahead of each analysis, a pre-processing of the samples was performed under vacuum at 300 °C for 3 h. The surface areas were calculated by the BET equation and the average pore diameter along with pore size distribution were determined by using the equivalent cylindrical model analysis of BJH.

X-ray fluorescence analysis (XRF) was implemented on an ARL-9800 apparatus to clear the bulk composition of the samples. The X-ray tube was operated at 60 kV and 20 mA.

X-ray photoelectron spectroscopy (XPS) analysis was performed on a PHI 5000 Versa Probe system, using monochromatic Al K (1486.6 eV) radiation operating at an accelerating power of 15 kW. Prior to the measurement, the samples were outgassed at room temperature in a UHV chamber ($<5 \times 10^{-7}$ Pa). All binding energies (BE) of the samples were calibrated with the adventitious C 1s peak at 284.6 eV to compensate the charging effect. The experimental error was within ±0.1 eV.

H_2-Temperature programmed reduction (H_2-TPR) was carried out with H_2–Ar mixture (7% H_2 by volume) as reducing agent. Typically, 50 mg sample was used in a quartz U-tube reactor for each measurement. After the sample was pre-treated in a N_2 stream at 200 °C for 0.5 h, reduction measurement of the sample by H_2 began from room temperature to 800 °C with a rate of 10 °C min^{-1}.

2.3 Catalytic activity test

The catalytic performance of the samples for NH_3-SCR reaction was determined under the reaction conditions as follows: 500 ppm NO, 500 ppm NH_3, 5 vol% O_2, 5 vol% H_2O (when used) and balance N_2. The total flow rate was 100 mL min^{-1} and

100 mg sample was put to use in a fixed-bed quartz reactor tube to get a space velocity of 60 000 mL g^{-1} h^{-1}. Before the mixture reactant gases were fed to the system, a preprocessing for the samples at 200 °C for 0.5 h was implemented to remove existent impurities, using high-purity N_2. The concentration of NO at designated temperature during the reaction was detected by an online Thermo fisher IS10 FTIR spectrometer equipped with a 2 m path-length gas cell (250 mL volume), through which NO conversion of the samples could be calculated in accordance with the following equations:

$$\text{NO conversion } (\%) = \frac{[\text{NO}]_{\text{in}} - [\text{NO}]_{\text{out}}}{[\text{NO}]_{\text{in}}} \times 100$$

$$\text{N}_2 \text{ selectivity } (\%) = \frac{[\text{NO}]_{\text{in}} - [\text{NO}]_{\text{out}} + [\text{NH}_3]_{\text{in}} - [\text{NH}_3]_{\text{out}} - [\text{NO}_2]_{\text{out}} - 2[\text{N}_2\text{O}]_{\text{out}}}{[\text{NO}]_{\text{in}} - [\text{NO}]_{\text{out}} + [\text{NH}_3]_{\text{in}} - [\text{NH}_3]_{\text{out}}} \times 100$$

3 Results and discussion

3.1 Morphology and structure

As presented in Fig. S1 (ESI†), uniform carbon spheres (CSs) with size of about 600 nm were obtained under hydrothermal condition. During hydrothermal process, dehydration, intermolecular cross-linking and nucleus growth are supposed to occur. As a result, carbon spheres with abundant superficial active functional groups (FT-IR, Fig. S2†) and accessible pore channels were formed.[29] Thus, target ions could be trapped easily on the surface of carbon spheres due to electrostatic force and diffuse inward through the channels. Sequentially, hollow structures were obtained after the following calcination process to remove the template. It was widely reported that different constituents and situations could give birth to varied hollow structures.[26,30,31] In the present work, mono-component and hybrid oxide hollow structures of manganese and cerium were prepared to explore the interaction between the constituents. Furthermore, the calcination rates were investigated for the tunable inner structures of the hybrid oxide hollow spheres.

The morphologies of as-synthesized samples were observed by SEM and TEM characterizations. As exhibited in Fig. 1b–d, after the calcination process under different conditions, multi-shell CeO_2–MnO_x hollow spheres (MSCMHSs) with sphere-in-sphere morphology were obtained. It was interesting that the inner structures of the hollow spheres could be controlled by changing the calcination rate, *i.e.*, single-shell (2 °C min^{-1}), double-shell (5 °C min^{-1}) and triple-shell (10 °C min^{-1}). The average diameter of the obtained MSCMHSs was about 400 nm, and the average shell thickness was 40 nm. Specially, the external, middle and internal shells of the triple-shell hollow spheres were approximately estimated as 400 nm, 150 nm and 50 nm, respectively. To further explore the elemental distribution of the multi-shell hollow spheres, HAADF-STEM was conducted on a single triple-shell hollow sphere as an example. Element mapping analysis in Fig. 2a showed that the triple-shell hollow structure could be discriminated clearly, in which the elements of Mn, Ce and O were distributed uniformly. It is worthy to be noted that the homogeneous elemental distribution of Mn and Ce was favorable to the synergistic effects between them. The HRTEM image and inset SAED pattern of triple-shell hollow sphere (Fig. 2b) demonstrated that the shell was polycrystalline. The lattice fringes with *d* spacing of 0.31 nm, 0.28 nm and 0.19 nm were ascribed to (111), (200), (220) crystal planes of fluorite-type CeO_2, respectively. Moreover, the lattice fringe of 0.25 nm was indexed to (202) crystal plane of Mn_3O_4. The diffraction rings and the inset XRD patterns accorded well with the crystalline phase results.

To shed light on the possible forming process of MSCMHSs, the morphology of CSs@CeO_2–MnO_x precursor before calcination was investigated. For that matter, the solvent-thermal treatment was believed as the critical step for MSCMHSs formation, which could efficiently enhance the adsorption and diffusion of manganese and cerium cations into the carbon spheres through the pore channels. As shown in Fig. S3† for the SEM image of the precursor after the solvent-thermal process, the spheres were uniformly dispersed with the size of approximately 600 nm as carbon spheres. The rough surface of the spheres containing tiny particles indicated the deposition of CeO_2–MnO_x precursor on the carbon spheres. Corresponding TEM image (Fig. 1a) displayed the core–shell architecture with the evident interface between CSs and CeO_2–MnO_x precursor. Notably, the MSCMHSs (Fig. 1b–d) exhibited smaller diameters than CSs@CeO_2–MnO_x precursor, which

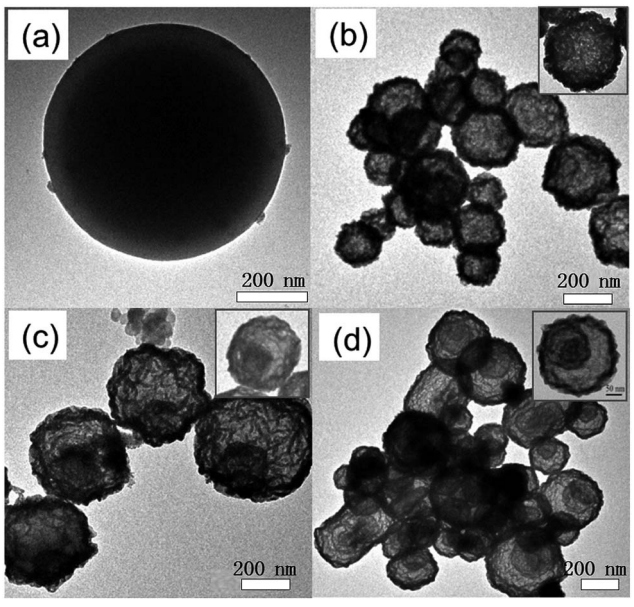

Fig. 1 TEM images of CeO_2–MnO_x hollow spheres with various shell number obtained at different heating rates: (a) before calcination; (b) single-shell, 2 °C min^{-1}; (c) double-shell, 5 °C min^{-1}; (d) triple-shell, 10 °C min^{-1}. Insets show the corresponding individual hollow sphere.

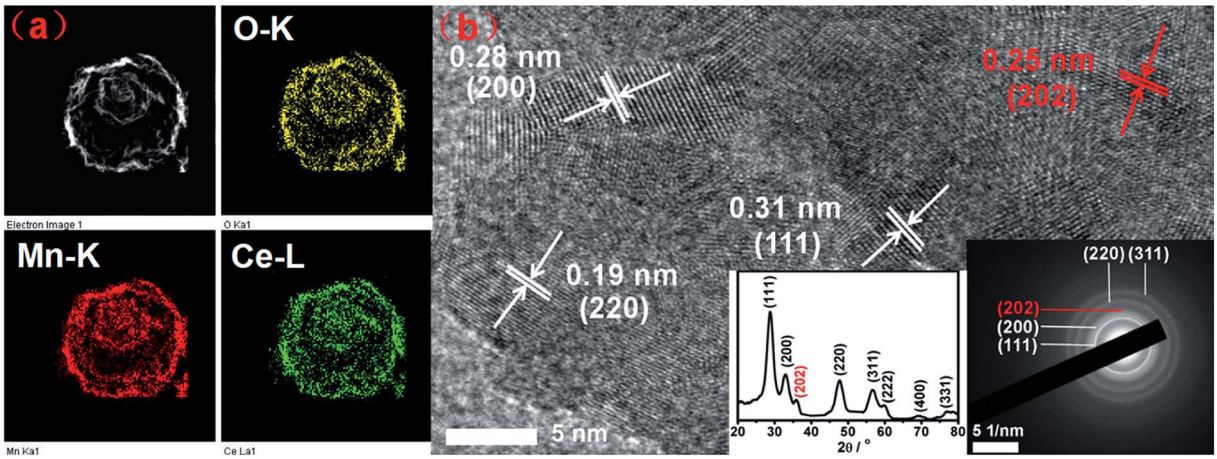

Fig. 2 (a) HAADF-STEM mapping images and (b) HRTEM image of the triple-shell hollow sphere. Insets are the corresponding XRD pattern and selected area electron diffraction (SAED) image.

revealed a shrinked process in accompany with combustion of carbon spheres during calcination. Besides, TG-DTA curves of the precursor were manifested in Fig. 3. Effects of different heating rates on the thermal process were investigated. There were two main exothermal peaks in the DTA curves for all cases. The exothermal peak around 250 °C and the sharp peak concentrated at around 320 °C derived from the combustion of carbon spheres.[11] Apparently, with the increasing heating rate, the intensity of exothermal peak for carbon spheres combustion increased. In particular, when the heating rate rose to 10 °C min^{-1} eventually, greatly enhanced exothermal intensity for carbon spheres combustion was observed. The results indicated that higher heating rate resulted in faster combustion of carbon spheres. As was reported,[32] the construction of multi-shell structure was mainly determined by the rate differences between oxide shell formation and carbon shrinkage, which

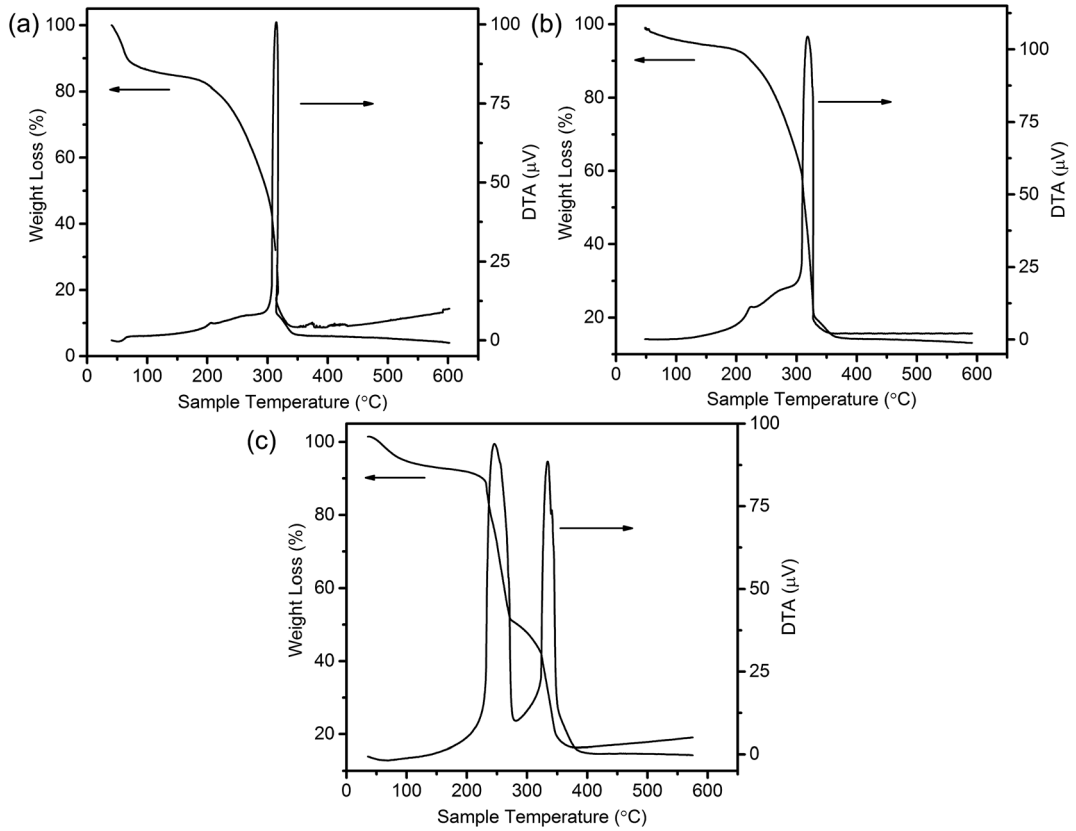

Fig. 3 TG-DTA curves of CSs@CeO_2–MnO_x precursor with different heating rates of (a) 2 °C min^{-1}, (b) 5 °C min^{-1} and (c) 10 °C min^{-1}.

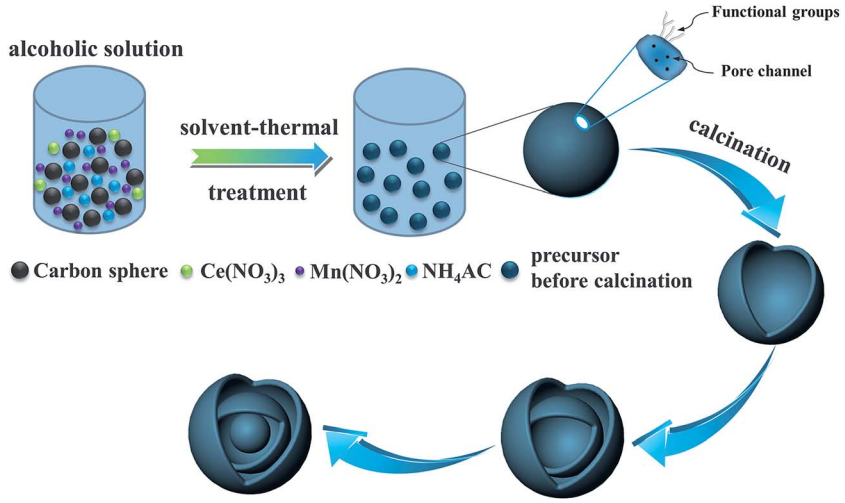

Scheme 1 Schematic diagram for synthesis of the MSCMHSs.

might cause separation. Therefore, with the increasing heating rate, a kind of heterogeneous contraction existed and facilitated the combustion of carbon spheres as well as the diffusion, penetration and redistribution of cations inward the carbon spheres. Thus, accompanied by different degrees of crystallization and penetration for manganese and cerium cations, controllable internal structures were obtained through the non-equilibrium calcination process,[21,33] with the removal of carbon spheres. The schematic diagram for synthesis of the MSCMHSs was illustrated in Scheme 1.

Additionally, the hollow spheres with single component (*i.e.*, Mn_2O_3 and CeO_2; confirmed by XRD patterns in Fig. 4) under calcination rate of 5 °C min^{-1} were synthesized (Fig. S4†). We could observe from the SEM image (Fig. S4a†) that Mn_2O_3 showed ruptured spherical structure with holes on the shell, which might be caused by airflow impact during calcination process. The ruptured structure and TEM image (Fig. S4c†) demonstrated its hollow characteristic, and it was noteworthy that double-shell hollow structures appeared. On the contrary, CeO_2 sample (Fig. S4b†) exhibited smoother surface and more complete spherical in shape with respect to those of Mn_2O_3, indicating stronger resistant ability to airflow impact for CeO_2. However, corresponding TEM image (Fig. S4d†) suggested that no double-shell structures were formed in CeO_2 hollow spheres. The result showed distinct behaviors between Mn_2O_3 and CeO_2 during the removing process of the templates. Otherwise, in the identical situations, CeO_2–MnO_x hybrid oxide possessed more complete spherical double-shell hollow structures than Mn_2O_3 and CeO_2, which indicated that hybrid oxide was conducive to forming complete multi-shell hollow structures due to synergistic interaction. Besides, considering of the structural properties of Mn_2O_3 and CeO_2 hollow spheres, it was proposed that the diffusivity between manganese and cerium elements inward carbon spheres was different. Occasionally, HAADF-STEM mapping images of one triple-shell hollow sphere with non-dispersed particles were captured. As shown in Fig. S5,† an aggregation state was detected from the non-dispersed particles outside the shells, which mainly consisted of O and Ce, with scarcely any Mn element. Therefore, combined with the widespread homogeneous dispersion of the elements in triple-shell hollow spheres, it was deduced that, under the synthesis process, the existence of Mn element was synergistically helpful for CeO_2 to diffuse inward carbon spheres, and then the multi-shell hollow structure was formed.

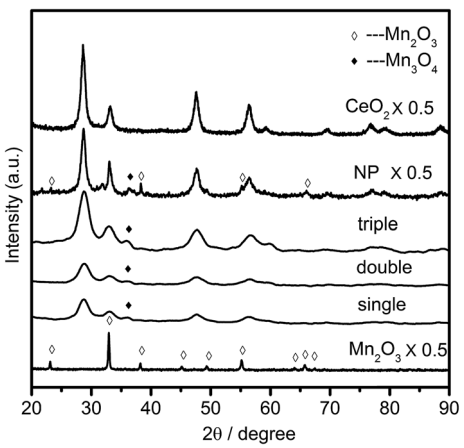

Fig. 4 XRD patterns of the samples.

The crystal structures of the samples were characterized by XRD, and the obtained patterns were displayed in Fig. 4. It was noted that the diffraction peaks of single component oxides of manganese and cerium were assigned to the characteristic reflections of Mn_2O_3 (bixbyite-C, JCPDS 31-0825) and CeO_2 (cubic fluorite, JCPDS 04-0593), respectively. While the hybrid multi-shell CeO_2–MnO_x hollow spheres (single, double and triple referred to the hollow structured samples with corresponding shells, respectively) all exhibited cubic fluorite-type CeO_2 phase (JCPDS 04-0593) together with a weak diffraction peak of tetragonal hausmannite Mn_3O_4 (JCPDS 08-0017) phase at around 36.0°. The result was in good consistency with the research finding upon CeO_2–MnO_x composites that when mole fraction of Mn was

Table 1 Textural properties of the samples

Samples	BET surface area ($m^2\ g^{-1}$)	Average pore diameter (nm)	Crystallite size (nm)
Mn_2O_3	22.6	3.50	28.8
Single	36.0	33.0	7.60
Double	30.0	31.5	6.50
Triple	35.0	30.8	5.20
NP	43.5	30.0	14.9
CeO_2	78.4	24.0	9.50

over than 50%, there appeared the crystalline phase of MnO_x.[16] Discrepancy of manganese crystalline phase for MSCMHSs (Mn_3O_4: Mn^{2+}, Mn^{3+}) and mono-component Mn_2O_3 hollow spheres (Mn^{3+}) might be caused by synergistic interactions between Mn and Ce elements ($Mn^{3+} + Ce^{3+} \leftrightarrow Mn^{2+} + Ce^{4+}$). Meanwhile, the constituents and calcination rates also had an effect on the crystallinity of the samples. For the identical calcination rates, Mn_2O_3 and CeO_2 hollow spheres both exhibited higher crystallinity compared with double-shell CeO_2–MnO_x hollow spheres. While with the identical constituents for MSCMHSs, higher calcination rates resulted in higher crystallinity. As listed in Table 1, crystallite sizes of samples were calculated by Scherrer equation based on the main diffraction peaks. It could be observed that the crystallite sizes for MSCMHSs were much smaller than that of Mn_2O_3 and CeO_2 hollow spheres due to the broader diffraction peaks. Furthermore, crystalline structure of the traditional CeO_2–MnO_x nanoparticles (NP) was investigated as well. As discerned in Fig. 4, except for the CeO_2 and Mn_3O_4 phase, NP possessed extra characteristic lines ascribed to Mn_2O_3 phase compared to MSCMHSs, indicating that template-assisted method could promote the dispersity of manganese species. Besides, the crystallite size of NP was estimated to be slightly larger than MSCMHSs.

3.2 Catalytic performance results

Selective catalytic reduction of NO with NH_3 was utilized to evaluate the catalytic performances of MSCMHSs as well as NP samples. The reaction was carried out at the space velocity of 60 000 mL g^{-1} h^{-1} over the temperature range from 100 °C to 275 °C. As disclosed in Fig. 5a, the NO conversion of all samples increased as the temperature increased and then decreased with different activated temperature windows. The MSCMHSs reached more than 90% conversion at temperatures as low as 125 °C, and it was noteworthy that hollow spheres with different number of shells exhibited different catalytic abilities. Among them, the triple-shell hollow spheres with a maintained conversion at 100% from 150 °C to 250 °C had the best performance. The NO conversion of double-shell hollow spheres was similar to that of the triple-shell ones from 100 °C to 200 °C but then decreased with the temperature increasing. Moreover, the single-shell hollow spheres showed the worst activity compared with the double-shell and triple-shell hollow spheres. However, it still displayed superior performance in contrast with NP, which could just achieve 84.3% conversion as the maximum activity value at 200 °C. Thus, an apparent enhancement in NO conversion for MSCMHSs than NP was observed within the range of testing temperature, indicating the positive role of multi-shell hollow structures in the reaction of NH_3-SCR, especially at low temperatures (100–150 °C). Otherwise, the N_2 selectivity of the samples declined gradually along with the rising temperature (Fig. 5b), this may due to the strong redox behavior of Mn-based catalysts, which could lead to the oxidation of NH_3 by O_2 to the by-product, for instance, NO_2 and N_2O.[34]

As discussed above, the catalytic performances of the samples ranked as the order of triple-shell > double-shell > single-shell > NP. Interestingly, the order of performances showed an inversed correlation with the crystalline sizes of the corresponding samples, just as the reports that smaller crystalline size was good for the enhanced activities.[35,36] Moreover, the superior catalytic activity of MSCMHSs might be attributed to the synergetic effect between active species of Mn and Ce elements.

To understand the H_2O resistance performance of the samples, the NH_3-SCR reaction under the condition with water

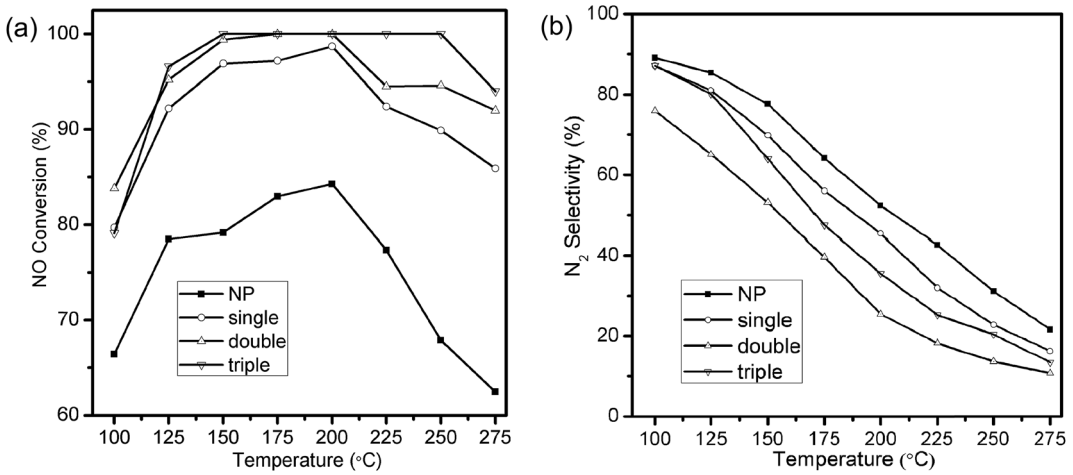

Fig. 5 (a) NO conversion and (b) N_2 selectivity of the samples as a function of temperature.

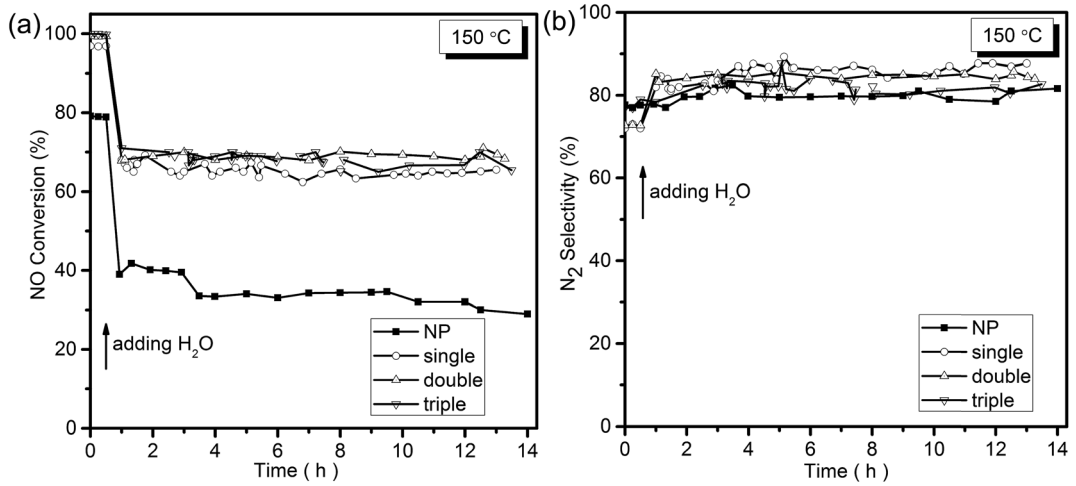

Fig. 6 (a) NO conversion and (b) N_2 selectivity of the samples as a function of temperature with the presence of water at 150 °C.

at 150 °C was performed. As displayed in Fig. 6a, after the H_2O was added into the mixture reactant gases, a decrease from 80% to less than 40% of NO conversation for NP samples was detected. At the same time, the NO conversation of the MCMSHSs declined as well but maintained at around 70% for more than 14 h, exhibiting better H_2O resistance performance than NP samples. It was obvious that the addition of H_2O caused deactivation of the samples in some degree, which could be explained that the adsorption of H_2O on the surface of the catalyst led to the formation of hydroxyl, resulting in a decline in activity.[37–39] Besides, an enhancement in N_2 selectivity (Fig. 6b) was also observed among the samples after the addition of H_2O, and this could be ascribed to the inhibition of H_2O to the oxidation of NH_3 by O_2.[38] To further investigate the key factor for the improved NH_3-SCR activity and the effects of special multi-shell hollow structures on the properties of the catalysts, characterizations of different samples were deeply examined.

3.3 N_2-Sorption characterization (BET)

N_2-Sorption isotherms were measured to get insights into the textural properties of the samples. It could be seen from Fig. 7a that all the isotherms of hollow spheres belonged to typical type-IV in the light of IUPAC classification, indicating the existence of mesoporous structure.[40] The observed H2-type hysteresis loops of CeO_2 hollow spheres manifested uniform pore structures. However, Mn_2O_3 and MCMSHSs possessed H3-type hysteresis loops, which might symbolize an irregular pore size distribution, just in keeping with pore distribution curves in Fig. 7b. It was noted that MSCMHSs samples showed similar broad pore size distribution with the average pore diameters being at around 30.0 nm. While Mn_2O_3 and CeO_2 hollow spheres exhibited narrower pore size distributions and smaller average pore diameters centered at 3.50 nm and 24.0 nm, respectively. As summarized in Table 1, there were no significantly differences among single-shell (36.0 m^2 g^{-1}), double-shell (30.0 m^2 g^{-1}) and triple-shell (35.0 m^2 g^{-1}) hollow spheres, which were smaller than 78.4 m^2 g^{-1} of CeO_2 but larger than 22.6 m^2 g^{-1} of Mn_2O_3. Thus, compared to mono-component oxides, the composite of manganese and cerium resulted in modifications on not only the inner structures but also the textural properties.

The adsorption–desorption isotherms and pore distribution curves of CeO_2–MnO_x nanoparticles (NP) was shown in Fig. 8. It was observed that, compared with MSCMHSs, NP showed a narrower pore size distribution while the same main distribution location. It could be explained by the removal of carbon spheres for the precursor during calcination, which might cause non-uniform pore size distribution of the obtained MCMSHSs, containing interstitial pores between the particles. Generally, the surface area of catalysts acted an important role in catalytic performance. However, despite the larger surface area (43.5 m^2 g^{-1}), NP exhibited poorer activity compared to MSCMHSs, which suggested that multi-shell hollow structures played more crucial roles in catalytic performances.

3.4 Bulk and surface analyses of the catalysts (XRF and XPS)

XRF characterization was performed to discover the bulk composition of the samples, and the result was summarized in Table 2. It could be found that the actual ratios of the two metal elements were approximately the same as the theoretical value for each sample, indicating the feasibility of the preparation process with negligible mass losses.

XPS was conducted to investigate the surface composition and existential state of active species on the samples. Herein, XPS spectra of the MSCMHSs and NP in Ce 3d, Mn 2p and O 1s regions were displayed in Fig. 9, with the peaks being fitted to several designated peaks based on the Gauss–Lorentz curves. The complicated Ce 3d spectrum of all the samples was separated into eight components with the allocation defined in Fig. 9a. The series of peaks labeled u were attributed to Ce $3d_{3/2}$ spin–orbit states, whereas those labeled v belonged to Ce $3d_{5/2}$ spin–orbit states. Specially, the two peaks signed as u′ and v′ represented Ce^{3+} species, and the other six peaks (u, v, u″, v″, u‴

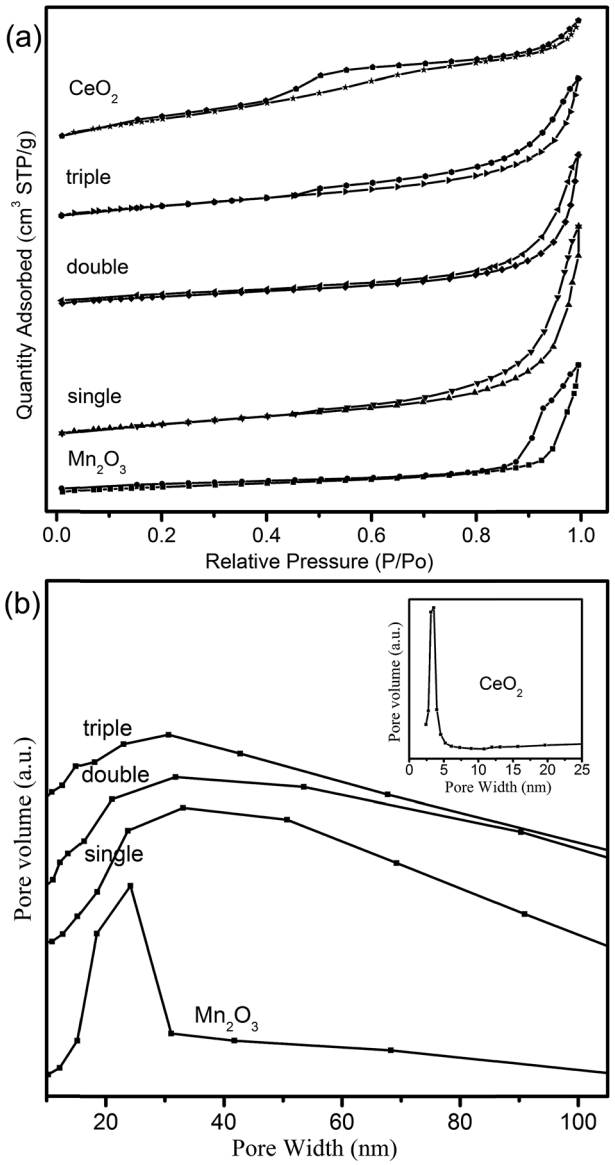

Fig. 7 (a) The N_2 adsorption/desorption isotherms and (b) BJH pore distribution curves of the hollow spheres (inset denotes CeO_2 hollow spheres).

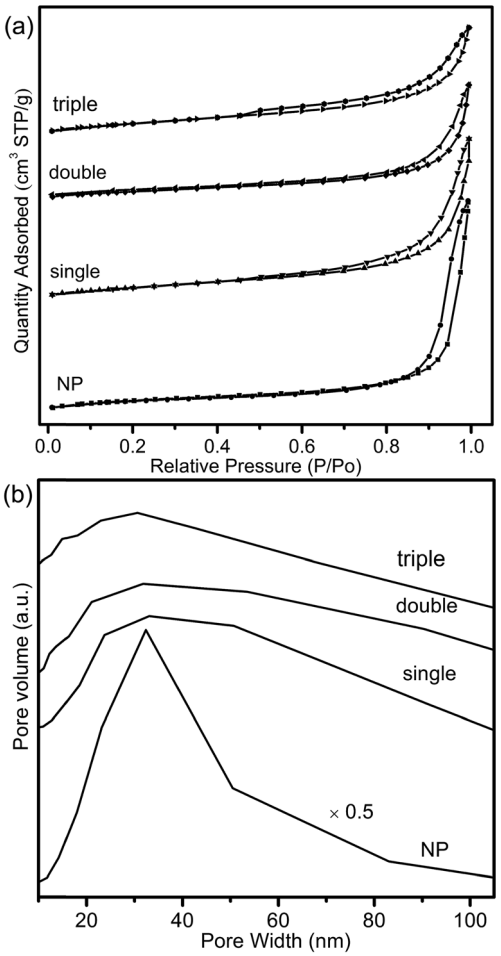

Fig. 8 (a) The N_2 adsorption/desorption isotherms and (b) BJH pore distribution curves of the composite CeO_2–MnO_x oxides.

Table 2 Bulk and surface atomic composition from XPS and XRF analyses

	Surface atomic ratio[a]			
Samples	$Ce^{3+}/(Ce^{4+} + Ce^{3+})$	$Mn^{4+}/(Mn^{4+} + Mn^{3+} + Mn^{2+})$	$O_\alpha/(O_\alpha + O_\beta)$	Bulk Mn/(Mn + Ce)[b]
NP	0.139	0.191	0.324	0.613
Single	0.165	0.214	0.370	0.644
Double	0.200	0.241	0.389	0.598
Triple	0.281	0.291	0.460	0.605

[a] Determined by XPS. [b] Determined by XRF (molar ratio).

and v‴) were ascribed to Ce^{4+} species.[41–43] It was obvious that both Ce^{3+} and Ce^{4+} species were co-existed in all the samples and the Ce^{4+} was the predominant chemical valence. In general, the existence of Ce^{3+} often led to the increase of active oxygen species on the surface of catalysts, which were in favor of the redox reaction.[44] Based on the fitting areas of the peaks, the ratios of $Ce^{3+}/(Ce^{4+} + Ce^{3+})$ of the samples were calculated and listed in Table 2, which ranked in the order of triple-shell > double-shell > single-shell > NP. The results suggested that, with the multi-shell hollow structures, MSCMHSs possessed more active Ce^{3+} species than NP, thus leading to the enhanced catalytic performance.

Fig. 9b exhibited two main peaks in Mn 2p spectrum of the samples at about 653.2 eV and 641.5 eV. There were mixed valences in manganese species on the surface of the samples, and the binding energies were overlapped. The peak at 653.2 eV was attributed to Mn $2p_{1/2}$ spin–orbit states, while the peak at 641.5 eV was due to Mn $2p_{3/2}$ spin–orbit states. As for Mn $2p_{3/2}$ spectrum, the peak was fitted to three characteristic peaks representing Mn^{2+} (640.7 eV), Mn^{3+} (642.1 eV) and Mn^{4+} (643.6 eV) species, respectively.[45,46] The existence of Mn^{2+} species for MSCMHSs proved the synergistic interaction between manganese and cerium oxide species, which was in good conformity

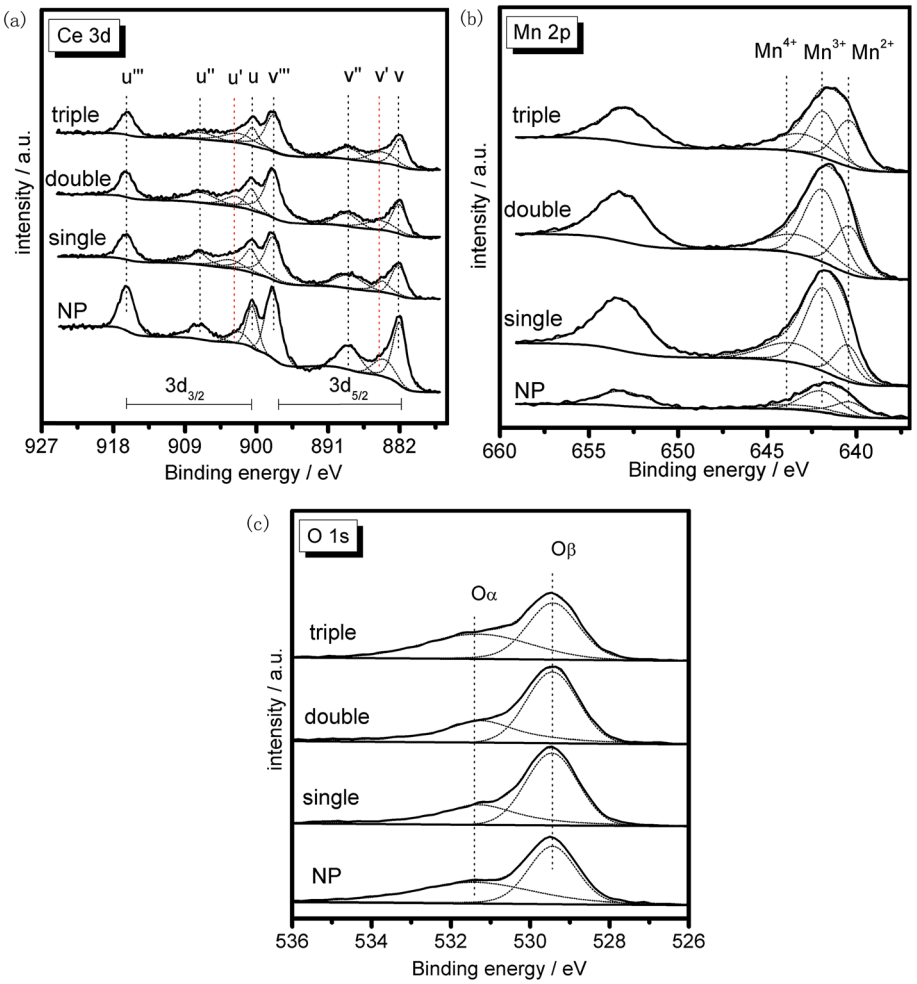

Fig. 9 XPS spectra of the samples in (a) Ce 3d, (b) Mn 2p and (c) O 1s regions.

with the results of XRD. Previous studies revealed that manganese species of higher oxidation state usually acted more important roles in redox reaction.[47] From Table 2, it was observed that the surface Mn^{4+} concentration of MSCMHSs were higher than NP. Especially, the triple-shell hollow spheres showed higher Mn^{4+} concentration than double-shell and single-shell hollow spheres. The result indicated the superiority of multi-shell hollow structures on surface active species, which was evidenced by the catalytic performances.

O 1s spectra of the samples (Fig. 9c) were ascribed to two overlapped peaks denoted as O_α (531.2–531.4 eV) and O_β (529.2–529.4 eV), respectively. Peak O_α with the higher binding energy was referred to the surface chemisorbed oxygen, correlated to the surface defects of samples.[48,49] While peak O_β was associated with lattice oxygen, bonding to the manganese or cerium cations.[50] Due to its remarkable mobility, O_α was regarded to be the most active oxygen species on the surface of catalysts.[51] Besides, the higher content of O_α relative to total oxygen concentration was able to bring better activity in oxidation reaction of NO to NO_2, which could accelerate the NH_3-SCR reaction through a "fast SCR" process.[52] The listed values of $O_\alpha/(O_\alpha + O_\beta)$ in Table 2 stated that the chemisorbed oxygen species of MSCMHSs were higher than NP just as that order of surface Ce^{3+} contents as well, accordant with the report that the existence of Ce^{3+} could trigger the formation of active oxygen species.[53]

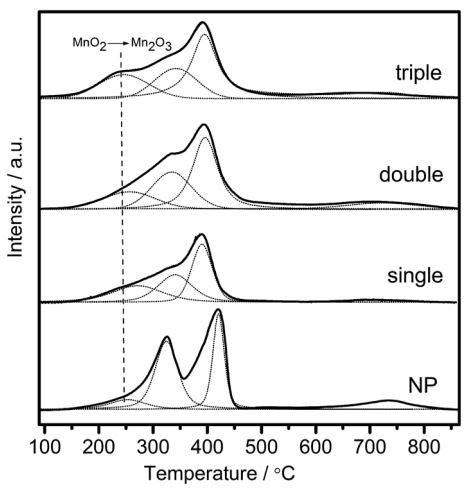

Fig. 10 H_2-TPR profiles of the samples as a function of temperature.

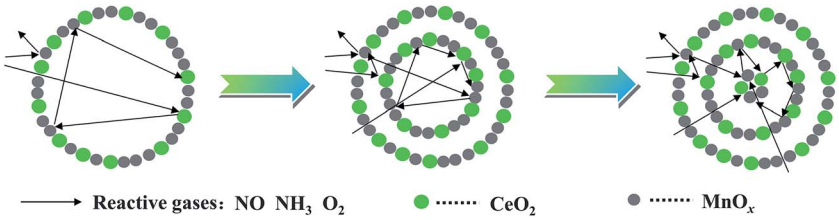

Fig. 11 Proposed collision processes of reactive gases against hollow spheres with different shells.

As manifested in above results of surface analysis, it was worth noting that the surface active species contents of the samples, which were beneficial to redox process, possessed the identical order with their catalytic performances. Hence, it seemed that the enriched surface active species of MSCMHSs could be essential for their better activities in SCR reaction compared with NP.

3.5 Redox performance

Redox performance of the catalysts that plays an important role in NH_3-SCR activity was measured by H_2-temperature programmed reduction (H_2-TPR) characterization. As demonstrated in Fig. 10, two series of broad reduction peaks could be obtained. In the case of lower temperature peak from 150 °C to 600 °C, two kinds of reduction were obtained, with one attributed to the step-by-step reduction of MnO_x species, and the other reduction of surface CeO_x species.[34] Besides, the peak at higher temperature from 700 °C to 800 °C corresponded to the reduction of bulk CeO_x species.[54] By means of the Gauss–Lorentz fitting, the lower-temperature broad reduction peak of all the samples was fitted to three reduction peaks characterized by apparent maxima at around 249, 330 and 410 °C, respectively. As reported,[16,34,55] the low-, middle-, and high-temperature reduction peak could be respectively attributed to the reduction of MnO_2 into Mn_2O_3, Mn_2O_3 into Mn_3O_4 and Mn_3O_4 into MnO, overlapped by reduction peak of surface Ce^{4+}. The discrepancy of redox performance showed that different preparation procedures brought about different interaction between manganese oxide and cerium oxide in the samples.[56] Compared with NP samples, the MCMSHSs, especially triple-shell ones, exhibited more superficial manganese species in a higher oxidation state (Mn^{4+}) and much broader reduction temperature range, which was consistent with the XPS analyses. Moreover, NP samples exhibited much higher Mn_2O_3 manganese species, just as shown in XRD characterization.

Moreover, the effect of unique hollow spheres on gases diffusion also acted an inspiring role in catalytic performances.[57] In contrast with NP, despite the smaller surface areas, it was considered that multi-shell hollow spheres with porous structures could promote gases diffusion into internal spaces. Thus, thorough contact of reactive gases with both internal and external of spheres was obtained, and then enhanced reactive surfaces were achieved. In addition, hollow spheres with more shells were demonstrated to be more effective to enhance the catalytic performances than those with fewer shells, which should be attributed to multiple collisions of reactive gases among different shells. As illustrated in Fig. 11, more effective collisions tended to appear in hollow structures with more shells, which exhibited richer surface active species as well. As a result, CeO_2–MnO_x catalysts with multi-shell hollow spherical morphology showed admired performances in NH_3-SCR reaction. The present study demonstrated that the well-designed morphology and structure offered an excellent strategy to the creation of highly efficient catalysts.

4 Conclusions

MSCMHSs with the average size of 400 nm were prepared successfully by the hard template method of carbon spheres, during which it was demonstrated that different calcination rate brought hollow spheres with different inner shell structures. The composite of manganese and cerium resulted in more complete hollow structures compared to monocomponent oxides, accompanied by modifications of crystalline phases, valence states and textural properties. Especially, the existence of Mn element could be helpful for CeO_2 to diffuse inward carbon spheres to form multi-shell hollow structures under experimental conditions. Furthermore, superior activities of MSCMHSs for NH_3-SCR reaction than traditional nanoparticles were displayed, and especially, triple-shell hollow spheres exhibited better performance than double-shell and single-shell ones, which could be attributed to the special structure and abundant surface active species, providing a new kind of material for low-temperature NH_3-SCR reaction.

Acknowledgements

The financial supports of the National Natural Science Foundation of China (No. 21273110, 21303082), the National High-tech R&D Program of China (863 program, No. 2015AA03A401) and Scientific Research Project of Environmental Protection Department of Jiangsu Province (2016048) are gratefully acknowledged.

References

1 L. Wang, F. Liu, W. Yang, H. Zhao, Y. Zheng, X. Chen and W. Dong, *Mater. Lett.*, 2013, **107**, 42–45.
2 S. Putla, M. H. Amin, B. M. Reddy, A. Nafady, K. A. Al Farhan and S. K. Bhargava, *ACS Appl. Mater. Interfaces*, 2015, **7**, 16525–16535.
3 A. Xie, J. Guo, W. Liu and Y. Yang, *RSC Adv.*, 2014, **4**, 11357.

4 J. Qi, K. Zhao, G. Li, Y. Gao, H. Zhao, R. Yu and Z. Tang, *Nanoscale*, 2014, **6**, 4072–4077.
5 S. Fang, Y. Xin, L. Ge, C. Han, P. Qiu and L. Wu, *Appl. Catal., B*, 2015, **179**, 458–467.
6 S. Andreoli, F. A. Deorsola and R. Pirone, *Catal. Today*, 2015, **253**, 199–206.
7 C. Tang, H. Zhang and L. Dong, *Catal. Sci. Technol.*, 2016, **6**, 1248–1264.
8 X. Yao, F. Gao, Q. Yu, L. Qi, C. Tang, L. Dong and Y. Chen, *Catal. Sci. Technol.*, 2013, **3**, 1355.
9 R. Qu, Y. Peng, X. Sun, J. Li, X. Gao and K. Cen, *Catal. Sci. Technol.*, 2016, **6**, 2136–2142.
10 P. Trogadas, J. Parrondo and V. Ramani, *Chem. Commun.*, 2011, **47**, 11549–11551.
11 P. Xu, R. Yu, H. Ren, L. Zong, J. Chen and X. Xing, *Chem. Sci.*, 2014, **5**, 4221–4226.
12 Z. Liu, Y. Liu, Y. Li, H. Su and L. Ma, *Chem. Eng. J.*, 2016, **283**, 1044–1050.
13 H. Hu, S. Cai, H. Li, L. Huang, L. Shi and D. Zhang, *ACS Catal.*, 2015, **5**, 6069–6077.
14 S. Cai, H. Hu, H. Li, L. Shi and D. Zhang, *Nanoscale*, 2016, **8**, 3588–3598.
15 W. Zhan, X. Zhang, Y. Guo, L. Wang, Y. Guo and G. Lu, *J. Rare Earths*, 2014, **32**, 146–152.
16 J. Quiroz, J.-M. Giraudon, A. Gervasini, C. Dujardin, C. Lancelot, M. Trentesaux and J.-F. Lamonier, *ACS Catal.*, 2015, **5**, 2260–2269.
17 F. Arena, *Catal. Sci. Technol.*, 2014, **4**, 1890.
18 L. Zhang, L. Shi, L. Huang, J. Zhang, R. Gao and D. Zhang, *ACS Catal.*, 2014, **4**, 1753–1763.
19 G. Chen, F. Rosei and D. Ma, *Adv. Funct. Mater.*, 2012, **22**, 3914–3920.
20 Y. Wei, Y. Sun, W. Su and J. Liu, *RSC Adv.*, 2015, **5**, 26231–26235.
21 L. Zhou, H. Xu, H. Zhang, J. Yang, S. B. Hartono, K. Qian, J. Zou and C. Yu, *Chem. Commun.*, 2013, **49**, 8695–8697.
22 B. Liu, Q. Wang, S. Yu, T. Zhao, J. Han, P. Jing, W. Hu, L. Liu, J. Zhang, L. D. Sun and C. H. Yan, *Nanoscale*, 2013, **5**, 9747–9757.
23 C. Sun, L. Liu, L. Qi, H. Li, H. Zhang, C. Li, F. Gao and L. Dong, *J. Colloid Interface Sci.*, 2011, **364**, 288–297.
24 W. Tian, C. Zhang, T. Zhai, S. L. Li, X. Wang, M. Liao, K. Tsukagoshi, D. Golberg and Y. Bando, *Chem. Commun.*, 2013, **49**, 3739–3741.
25 H. Zhao, J.-F. Chen, Y. Zhao, L. Jiang, J.-W. Sun and J. Yun, *Adv. Mater.*, 2008, **20**, 3682–3686.
26 J. Wang, N. Yang, H. Tang, Z. Dong, Q. Jin, M. Yang, D. Kisailus, H. Zhao, Z. Tang and D. Wang, *Angew. Chem., Int. Ed.*, 2013, **52**, 6417–6420.
27 S. Liu, M. Xie, X. Guo and W. Ji, *Mater. Lett.*, 2013, **105**, 192–195.
28 L. C. Liu, Q. Fan, C. Z. Sun, X. R. Gu, H. Li, F. Gao, Y. F. Chen and L. Dong, *J. Power Sources*, 2013, **221**, 141–148.
29 X. Sun and Y. Li, *Angew. Chem., Int. Ed.*, 2004, **43**, 597–601.
30 M. H. Oh, T. Yu, S.-H. Yu, B. Lim, K.-T. Ko, M.-G. Willinger, D.-H. Seo, B. H. Kim, M. G. Cho, J.-H. Park, K. Kang, Y.-E. Sung, N. Pinna and T. Hyeon, *Science*, 2013, **340**, 964–968.
31 J. Wang, H. Tang, H. Ren, R. Yu, J. Qi, D. Mao, H. Zhao and D. Wang, *Adv. Sci.*, 2014, **1**, 1400011.
32 X. Lai, J. Li, B. A. Korgel, Z. Dong, Z. Li, F. Su, J. Du and D. Wang, *Angew. Chem.*, 2011, **50**, 2738–2741.
33 J. Guan, F. Mou, Z. Sun and W. Shi, *Chem. Commun.*, 2010, **46**, 6605–6607.
34 Y. Xiong, C. Tang, X. Yao, L. Zhang, L. Li, X. Wang, Y. Deng, F. Gao and L. Dong, *Appl. Catal., A*, 2015, **495**, 206–216.
35 P. R. Ettireddy, N. Ettireddy, T. Boningari, R. Pardemann and P. G. Smirniotis, *J. Catal.*, 2012, **292**, 53–63.
36 F. Liu, H. He, C. Zhang, Z. Feng, L. Zheng, Y. Xie and T. Hu, *Appl. Catal., B*, 2010, **96**, 408–420.
37 S. Pan, H. Luo, L. Li, Z. Wei and B. Huang, *J. Mol. Catal. A: Chem.*, 2013, **377**, 154–161.
38 S. Xiong, Y. Liao, X. Xiao, H. Dang and S. Yang, *Catal. Sci. Technol.*, 2015, **5**, 2132–2140.
39 Z. Lei, B. Han, K. Yang and B. Chen, *Chem. Eng. J.*, 2013, **215–216**, 651–657.
40 K. S. W. Sing, D. H. Everett, R. A. W. Haul, L. Moscou, R. A. Pierotti, J. Rouquerol and T. Siemieniewska, *Pure Appl. Chem.*, 1985, **57**, 603–619.
41 S. Watanabe, X. Ma and C. Song, *J. Phys. Chem. C*, 2009, **113**, 14249–14257.
42 P. Hartmann, T. Brezesinski, J. Sann, A. Lotnyk, J.-P. Eufinger, L. Kienle and J. Janek, *ACS Nano*, 2013, **7**, 2999–3013.
43 S. M. Lee and S. C. Hong, *Appl. Catal., B*, 2015, **163**, 30–39.
44 S. Yang, W. Zhu, Z. Jiang, Z. Chen and J. Wang, *Appl. Surf. Sci.*, 2006, **252**, 8499–8505.
45 X. Tang, Y. Li, X. Huang, Y. Xu, H. Zhu, J. Wang and W. Shen, *Appl. Catal., B*, 2006, **62**, 265–273.
46 G. C. Allen, S. J. Harris, J. A. Jutson and J. M. Dyke, *Appl. Surf. Sci.*, 1989, **37**, 111–134.
47 J. S. Park, D. S. Doh and K.-Y. Lee, *Top. Catal.*, 2000, **10**, 127–131.
48 G. Carja, Y. Kameshima, K. Okada and C. D. Madhusoodana, *Appl. Catal., B*, 2007, **73**, 60–64.
49 S. Wu, X. Yao, L. Zhang, Y. Cao, W. Zou, L. Li, K. Ma, C. Tang, F. Gao and L. Dong, *Chem. Commun.*, 2015, **51**, 3470–3473.
50 B. M. Reddy, P. Bharali, P. Saikia, S.-E. Park, M. W. E. van den Berg, M. Muhler and W. Grunert, *J. Phys. Chem. C*, 2008, **112**, 11729–11737.
51 L. Jing, Z. Xu, X. Sun, J. Shang and W. Cai, *Appl. Surf. Sci.*, 2001, **180**, 308–314.
52 W. Shan, F. Liu, H. He, X. Shi and C. Zhang, *Chem. Commun.*, 2011, **47**, 8046–8048.
53 Z. Zou, M. Meng, L. Guo and Y. Zha, *J. Hazard. Mater.*, 2009, **163**, 835–842.
54 H. C. Yao and Y. F. Y. Yao, *J. Catal.*, 1984, **86**, 254–265.
55 J. Q. Torres, J.-M. Giraudon and J.-F. Lamonier, *Catal. Today*, 2011, **176**, 277–280.
56 C. Fang, D. Zhang, L. Shi, R. Gao, H. Li, L. Ye and J. Zhang, *Catal. Sci. Technol.*, 2013, **3**, 803–811.
57 C. Song, C. Wang, H. Zhu, X. Wu, L. Dong and Y. Chen, *Catal. Lett.*, 2008, **120**, 215–220.